https://doi.org/10.1016/j.ymssp.2016.12.005

A Diagnostic Imaging Approach for Online Characterization of Multi-impact in Aircraft Composite Structures based on a Scanning Spatial-Wavenumber Filter of Guided Wave

Yuanqiang Ren[1], **Lei Qiu**[1*,2], **Shenfang Yuan**[1], **Zhongqing Su**[2*]

1 Research Center of Structural Health Monitoring and Prognosis, State Key Lab of Mechanics and Control of Mechanical Structures, Nanjing University of Aeronautics and Astronautics, Nanjing 210016, P. R. China.

2 Department of Mechanical Engineering, Hong Kong Polytechnic University, Kowloon, Hong Kong.

* Corresponding author: Lei Qiu, Email: lei.qiu@nuaa.edu.cn; Zhongqing Su, Email: mmsu@polyu.edu.hk

Abstract:

Monitoring of impact and multi-impact in particular in aircraft composite structures has been an intensive research topic in the field of guided-wave-based structural health monitoring (SHM). Compared with the majority of existing methods such as those using signal features in the time-, frequency- or joint time-frequency domain, the approach based on spatial-wavenumber filter of guided wave shows superb advantage in effectively distinguishing particular wave modes and identifying their propagation direction relative to the sensor array. However, there exist two major issues when conducting online characterization of multi-impact event. Firstly, the spatial-wavenumber filter should be realized in the situation that the wavenumber of high spatial resolution of the complicated multi-impact signal cannot be measured or modeled. Secondly, it's difficult to identify the multiple impacts and realize multi-impact localization due to the overlapping of wavenumbers. To address these issues, a scanning spatial-wavenumber filter based diagnostic imaging method for online characterization of multi-impact event is proposed to conduct multi-impact imaging and localization in this paper. The principle of the scanning filter for multi-impact is developed first to conduct spatial-wavenumber filtering and to achieve wavenumber-time imaging of the multiple impacts. Then, a feature identification method of multi-impact based on eigenvalue decomposition and wavenumber searching is presented to estimate the number of impacts and calculate the wavenumber of the multi-impact signal, and an image mapping method is proposed as well to convert the wavenumber-time image to an angle-distance image to distinguish and locate the multiple impacts. A series of multi-impact events are applied to a carbon fiber laminate plate to validate the proposed methods. The validation results show that the localization of the multiple impacts are well achieved.

Keywords: aircraft composite structure; structural health monitoring; impact imaging; guided wave; spatial-wavenumber filter.

1. Introduction

Due to the superior characteristics over conventional materials, composite materials have been gradually adopted in aerospace industry [1-5]. However, the poor impact resistance of such materials may lead to barely visible impact damages and result in stiffness degradation and a significant loss of structural integrity. Therefore impact monitoring of aircraft composite structures is an important research topic in the field of Structural Health Monitoring (SHM).

In the last twenty years, many researchers have been interested in taking advantages of guided wave and piezoelectric (referred as PZT in the rest of this paper) sensor to realize impact monitoring of composite structures [6-11]. In early studies, different kinds of methods have been proposed to realize impact localization and impact energy estimation from the perspective of geometry or mechanics model [12-14]. However, in order to improve signal-to-noise ratio and achieve high accuracy and tolerance of impact localization on real aircraft structures, many studies began to introduce PZT array based imaging techniques to impact localization in recent years, such as impact energy imaging [15-16], time-reversal imaging [17-21], multiple signal classification [22-23]. These methods researched till now have shown the practical application potential of impact imaging techniques based on guided wave in aerospace industry [24-26].

All the literatures mentioned above concentrate on processing guided wave in time domain, frequency domain or time-frequency domain. Comparing with those methods, the spatial-wavenumber filter has been proved to be an effective approach to distinguish propagating direction and different modes of the guided wave, and has been widely researched with a lot of well-performed work published in recent years [27-30]. However, in most of these studies, the wavenumber with high spatial resolution of narrow-band guided wave signal needs to be measured first by using a laser Doppler vibrometer as a spatial sampling device. That is the main reason why these methods can only be applied to off-line damage inspection at the current stage. To improve the feature of on-line monitoring of spatial-wavenumber filter, Purekar et al. [31] and Wang et al. [32] developed on-line damage imaging methods by taking a linear PZT array instead of a laser Doppler vibrometer as a spatial sampling device but an accurate wavenumber curve must be modeled or measured beforehand in order to perform the spatial-wavenumber filter. These abovementioned researches all concentrate on realizing damage inspection or monitoring by using the spatial-wavenumber filter.

It is well known that impact is a kind of instant event and needs to be monitored on-line continuously.

Besides, aircraft composite structures are often struck by multiple impacts occurring simultaneously. This situation may be encountered when an aircraft is passing through a region with rain, dust or hail, which results in multiple damages on the structure [22, 33-34]. Thus it is important and necessary to develop a spatial-wavenumber filter based multi-impact imaging method for aircraft composite structures.

Regarding the on-line impact monitoring combining with the spatial-wavenumber filter, several preliminary progresses have been made. Baravelli et al. [35] proposed a guided wave transducer of wavenumber frequency-steerable combing with spatial-wavenumber imaging, and multiple sources imaging of guided wave was realized. However, the sources were only simulated by taking PZT sensors as the excitation. Under this situation, the problem of how to determine the impact occurring time was avoided because the excitation time can be recorded beforehand, but the impact occurring time cannot. In addition, the source localization was only performed on an aluminum plate and the localization accuracy needed to be further improved. In the authors' previous study [36], a model-independent spatial-wavenumber filter based impact imaging and localization method was proposed to achieve impact monitoring without wavenumber measuring or modeling. By extracting frequency narrow-band signal from the wideband impact response signal, the method realized the one-to-one relationship between the wavenumber of the signal and its propagating direction, and was able to locate impact on composite structures without blind angle. However, the method was only applied to single impact imaging. Besides, the impact localization result wasn't given by the spatial-wavenumber image directly and a geometrical localization method needed to be used, which reduced the localization accuracy.

To develop an on-line multi-impact imaging method based on spatial-wavenumber filter for aircraft composite structures, some issues must be addressed.

(1) The spatial-wavenumber filtering of multi-impact signal should be realized in the situation that the wavenumber of high spatial resolution of the complicated impact signals cannot be measured or modeled.

(2) Due to the overlapping of guided wave wavenumbers when multiple impacts occurring simultaneously, it's difficult to identify the multiple impacts and realize multi-impact localization.

In this paper, a scanning spatial-wavenumber filter based diagnostic imaging method for online characterization of multi-impact event is proposed to conduct multi-impact imaging and localization, based on the authors' previous study [36]. With this method, a PZT 2D cross-shaped array which consists of two orthogonal linear PZT arrays is adopted to fulfill the spatial sampling of the multi-impact signal. The principle of the spatial-wavenumber filter for multiple impacts of guided wave is developed and a scanning

spatial-wavenumber filter is proposed to realize the spatial-wavenumber filtering of the multi-impact signal without wavenumber measuring or modeling. The continuous complex Shannon wavelet transform is used to extract the frequency narrow-band component of the multi-impact signal. By applying the scanning spatial-wavenumber filter to the multi-impact signal of frequency narrow-band, the wavenumber-time images of the multiple impacts can be obtained first. Then a feature identification method of multi-impact based on eigenvalue decomposition and wavenumber searching is proposed to estimate the number of impacts and the wavenumber of the multi-impact signal. Based on the result, an image mapping method is presented to convert the wavenumber-time images to an angle-distance image to distinguish and locate the multiple impacts. Finally, the proposed multi-impact imaging and localization method is validated on a carbon fiber laminate plate and the validation results are discussed in detail with different multi-impact cases.

The rest of this paper is organized as follows. In Section 2, the spatial sampling of multi-impact signal is discussed, followed by the design of the scanning spatial-wavenumber filter for multi-impact. In section 3, the multi-impact imaging and localization method is proposed, including the feature identification method of multiple impacts and the mapping method from wavenumber-time images to an angle-distance image. Section 4 gives the experimental validation. Finally, conclusions are presented in Section 5.

2. The scanning spatial-wavenumber filter for multi-impact

2.1 Spatial sampling of multi-impact signal

The on-line implementation of the spatial-wavenumber filter relies on a linear PZT array which is composed of M PZTs with a distance of τ between two adjacent ones, as shown in Fig. 1. Taken the center point of the linear PZT array as the pole, a polar coordinate system is built and the linear PZT array is along the 0° direction. The polar coordinate of the No. m ($1 \leq m \leq M$) PZT is expressed as Eq. (1).

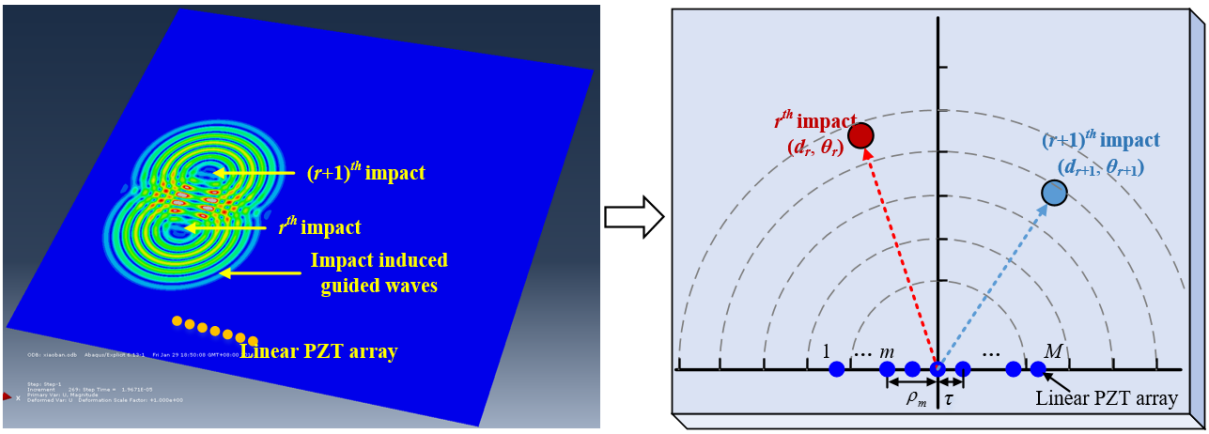

Fig. 1 Schematic diagram of the spatial sampling based on a linear PZT array

$$\left(\rho_m,\theta_m\right)=\begin{cases}\left(\tau\cdot\left|m-\dfrac{M+1}{2}\right|,\pi\right) & m<\dfrac{M+1}{2}\\ (0,0) & m=\dfrac{M+1}{2}\\ \left(\tau\cdot\left|m-\dfrac{M+1}{2}\right|,0\right) & m>\dfrac{M+1}{2}\end{cases} \tag{1}$$

Assuming that R impacts occur at the same time and generate multi-impact signal propagating on the structure, as shown in Fig.1. The distance and angle of the r^{th} ($1\le r\le R$) impact relative to the pole are denoted as d_r and θ_r respectively. It should be noted that the multi-impact signal is composed of the guided waves induced by different impacts.

The linear PZT array is used to acquire the multi-impact signal which is frequency wideband. However, the spatial-wavenumber filter based impact monitoring method requires the signal to be frequency narrow-band [36]. This point is important for multi-impact monitoring because different impacts may induce the guided waves of different frequency bands. Under this situation, the one-to-one relationship between the wavenumber and the impact direction is hard to be satisfied. In this paper, the continuous complex Shannon wavelet transform is adopted to extract the frequency narrow-band signal from the multi-impact signal [18]. The extracted frequency narrow-band signal with a central frequency ω_c of the No. m PZT can be expressed as Eq. (2) [4, 37-38].

$$s\left(\rho_m,t\right)=\sum_{r=1}^{R} f_m^r(t)\cdot e^{i\cdot\omega_c\cdot t}\cdot e^{-i\cdot\xi_c\cdot\left|\vec{\boldsymbol{d}}_r-\vec{\boldsymbol{\rho}}_m\right|} \tag{2}$$

Where $f_m^r(t)$ is the amplitude of the signal caused by the r^{th} impact, ξ_c is the wavenumber corresponding to ω_c, $\vec{\boldsymbol{d}}_r$ and $\vec{\boldsymbol{\rho}}_m$ denote the distance vector of d_r and ρ_m respectively.

Based on the frequency narrow-band extraction, the wavenumbers of guided waves induced by different impacts are approximately equal with each other. In this paper, only the frequency narrow-band signal is taken into account, thus the multi-impact signal in the rest of the paper is considered to be a frequency narrow-band signal.

To simplify Eq. (2), the phase change of the signal $\left|\vec{\boldsymbol{d}}_r-\vec{\boldsymbol{\rho}}_m\right|$ is represented by its second-order Taylor expansion, as shown in Eq. (3).

$$\left|\vec{\boldsymbol{d}}_r-\vec{\boldsymbol{\rho}}_m\right|=d_r-\rho_m\cdot\cos\theta_r+\frac{\rho_m^2\cdot\left(\sin\theta_r\right)^2}{2d_r}+O\left(\rho_m^3\right) \tag{3}$$

In a far-field situation, the wave fronts of the multi-impact signal arrive at the PZT array in a planar way, which means that the term of second-order in Eq. (3) can be ignored [39-40]. Besides, considering that the distance between different PZTs are very small compared to the distance of impact, the signal amplitudes of different PZTs caused by the r^{th} impact are approximately equal and denoted as $f^r(t)$, as shown in Eq. (4). Thus Eq. (2) can be approximately converted to Eq. (5).

$$f^r(t) = f_1^r(t) \approx \cdots \approx f_m^r(t) \approx \cdots \approx f_M^r(t) \tag{4}$$

$$s(\rho_m, t) = \sum_{r=1}^{R} f^r(t) \cdot e^{i\cdot\omega_c\cdot t} \cdot e^{-i\cdot\xi_c\cdot d_r} \cdot e^{i\cdot\xi_c\cdot\cos\theta_r\cdot\rho_m} \tag{5}$$

To perform the spatial-wavenumber filtering, the linear PZT array is used as a spatial sampling device with a sampling rate of $2\pi/\tau$. The spatial sampling signal of the multi-impact, namely the multi-impact signal at time point t, can be expressed as Eq. (6).

$$\boldsymbol{s}(\rho, t) = \left[s(\rho_1, t), s(\rho_2, t), \cdots, s(\rho_m, t), \cdots, s(\rho_M, t) \right] \tag{6}$$

By using the Discrete Fast Fourier Transform (DFFT), the spatial sampling signal can be transformed to the wavenumber domain, as shown in Eq. (7) and Eq. (8).

$$S(\xi, t) = \sum_{\rho=\rho_1}^{\rho_M} \sum_{r=1}^{R} f^r(t) \cdot e^{i\cdot\omega_c\cdot t} \cdot e^{-i\cdot\xi_c\cdot d_r} \cdot e^{i\cdot\xi_c\cdot\cos\theta_r\cdot\rho} \cdot e^{-i\xi\rho} = \sum_{r=1}^{R} 2\pi \cdot \Psi^r(t) \cdot \delta(\xi - \xi_c \cdot \cos\theta_r) \tag{7}$$

$$\Psi^r(t) = f^r(t) \cdot e^{i\cdot\omega_c\cdot t} \cdot e^{-i\cdot\xi_c\cdot d_r} \tag{8}$$

Where $\delta(x)$ is the Dirac function given by Eq. (9).

$$\delta(x) = \begin{cases} 1 & x = 0 \\ 0 & x \neq 0 \end{cases} \tag{9}$$

Eq. (7) and Eq. (9) indicate when R impacts occurring at the same time, the spatial sampling signal has R wavenumbers, in which the r^{th} wavenumber $\xi_c \cdot cos\theta_r$ is the projection wavenumber of the r^{th} impact with angle θ_r on the linear PZT array. The wavenumber spectrum of the spatial sampling signal of the linear PZT array contains R projection wavenumbers corresponding to the R impacts.

2.2 The scanning spatial-wavenumber filter

According to the wavenumber spectrum of the spatial sampling signal mentioned above, a spatial-wavenumber filter can be designed based on the linear PZT array. The designed spatial-wavenumber filter is given by Eq. (10) and (11).

$$\boldsymbol{\phi}(\rho,\xi_n)=\left[\phi(\rho_1,\xi_n),\phi(\rho_2,\xi_n),\cdots,\phi(\rho_m,\xi_n),\cdots,\phi(\rho_M,\xi_n)\right] \tag{10}$$

$$\phi(\rho_m,\xi_n)=e^{i\cdot\xi_n\cdot\rho_m} \tag{11}$$

Where ξ_n is the central wavenumber of the filter. By using DFFT, the wavenumber spectrum of the filter can be expressed as Eq. (12). It indicates that the filter is able to selectively allow the signal with the wavenumber of ξ_n to pass, while reject the signals with other wavenumbers.

$$\Phi(\xi)=2\pi\delta(\xi-\xi_n) \tag{12}$$

In actual situation, the wavenumber ξ_c cannot be known beforehand without modeling or measuring. Thus, a series of spatial-wavenumber filters of different central wavenumbers are designed to construct a matrix of spatial-wavenumber filters as given in Eq. (13) to scan the spatial sampling signal from $-\xi_{max}$ to ξ_{max} to get ξ_c. The matrix of the spatial-wavenumber filters is called as the scanning spatial-wavenumber filter.

$$\boldsymbol{\phi}(\rho,\xi_n)=\begin{bmatrix}\phi(\rho_1,\xi_1) & \phi(\rho_2,\xi_1) & \cdots & \phi(\rho_M,\xi_1)\\ \phi(\rho_1,\xi_2) & \phi(\rho_2,\xi_2) & \cdots & \phi(\rho_M,\xi_2)\\ \vdots & \vdots & \ddots & \vdots\\ \phi(\rho_1,\xi_N) & \phi(\rho_2,\xi_N) & \cdots & \phi(\rho_M,\xi_N)\end{bmatrix}_{N\times M} \tag{13}$$

Where ξ_{max} is the maximum scanning wavenumber of the scanning spatial-wavenumber filter and should be less than half of the spatial sampling rate, as shown in Eq. (14). N is the maximum scanning step, calculated by Eq. (15). $\Delta\xi$ is the scanning resolution. The wavenumber ξ_n of the filter is expressed as Eq. (16).

$$\xi_{\max}<\frac{1}{2}\cdot\frac{2\pi}{\tau}=\frac{\pi}{\tau} \tag{14}$$

$$N=\frac{\xi_{\max}-\left(-\xi_{\max}\right)}{\Delta\xi}+1=\frac{2\xi_{\max}}{\Delta\xi}+1 \tag{15}$$

$$\xi_n=-\xi_{\max}+(n-1)\Delta\xi,\ \ n=1,2,\cdots,N \tag{16}$$

After applying the scanning spatial-wavenumber filter to the spatial sampling signal, the scanning filtering response is expressed as Eq. (17).

$$\boldsymbol{H}(t,\xi_n)=\boldsymbol{s}(\rho,t)\otimes\boldsymbol{\phi}(\rho,\xi_n)^T=\sum\left|\boldsymbol{s}(\rho,t)\times\boldsymbol{\phi}(\rho,\xi_n)^T\right|=\left|\sum_{r=1}^{R}4\pi^2\cdot\Psi^r\cdot\delta(\xi_n-\xi_c\cdot\cos\theta_r)\right| \tag{17}$$

The scanning process of the filter is shown in Fig. 2. For a scanning wavenumber ξ_n, if $\xi_n=\xi_c\cdot\cos\theta_r$, which means that the scanning wavenumber is equal to the projection wavenumber of the r^{th} impact on the linear PZT array, the corresponding spatial sampling signal of the r^{th} impact is able to pass the filter, resulting in a peak value of $\boldsymbol{H}(t, \xi_n)$. If $\xi_n\neq\xi_c\cdot\cos\theta_r$, the spatial sampling signal is unable to pass the filter, resulting in a

small value of $\boldsymbol{H}(t, \xi_n)$. According to this point, the projection wavenumbers on the linear PZT array of the spatial sampling signal can be obtained.

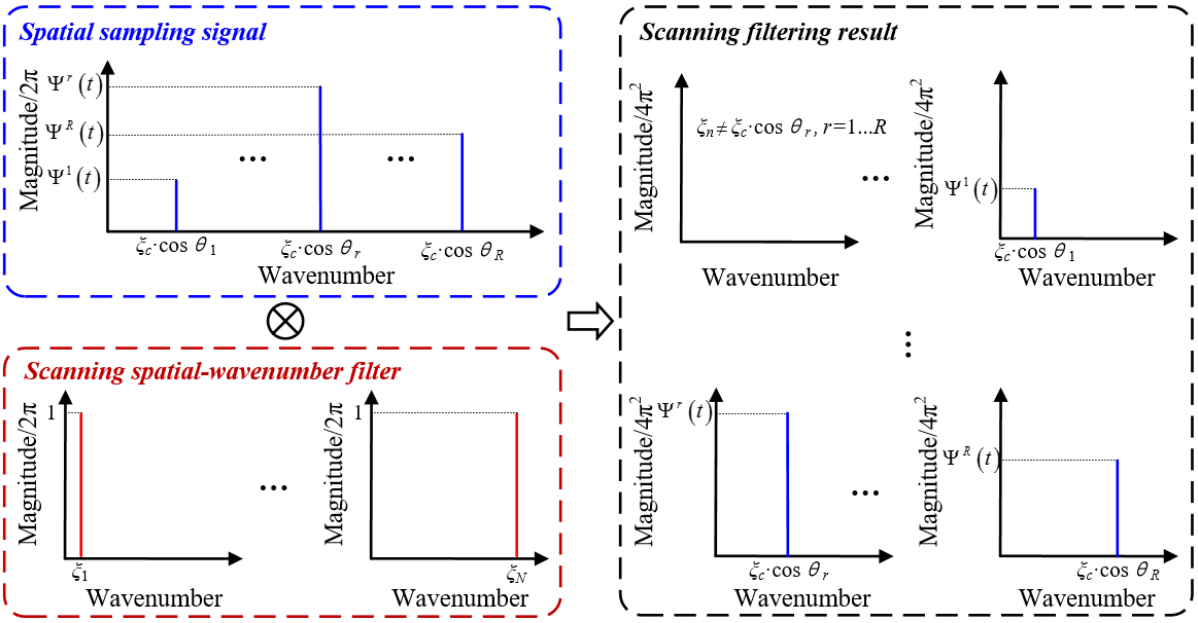

Fig. 2 Schematic of the scanning spatial-wavenumber filter for multi-impact

3. The multi-impact imaging and localization method

Based on the research mentioned above, the multi-impact imaging and localization method is proposed to locate the multi-impact event. In this section, the descriptions of different parts of the method are given out respectively, then an overview of the method is summarized.

3.1 Wavenumber-time imaging of multiple impacts

In Section 2, the scanning spatial-wavenumber filter is designed based on a linear PZT array. For multi-impact imaging, a PZT 2D cross-shaped array is adopted, as shown in Fig. 3, which is composed of two orthogonal linear PZT arrays labeled as No. I and No. II. A polar coordinate system is built based on the PZT 2D cross-shaped array and the pole is set to be the central point of the array. PZT array I is along the 0° direction and PZT array II is along the 90° direction.

For each of the two arrays, a scanning spatial-wavenumber filter can be designed to filter the spatial sampling signal, namely the multi-impact signal at time t, to get the scanning filtering response $\boldsymbol{H}(t, \xi_n)$. Assuming the duration time of the multi-impact signal is T, then a scanning matrix $\mathbf{H}$ can be obtained by filtering all the spatial sampling signals $\mathbf{s}$ from time 0 to time T, as shown in Fig. 4. By imagining the scanning matrix $\mathbf{H}$, a wavenumber-time image is generated.

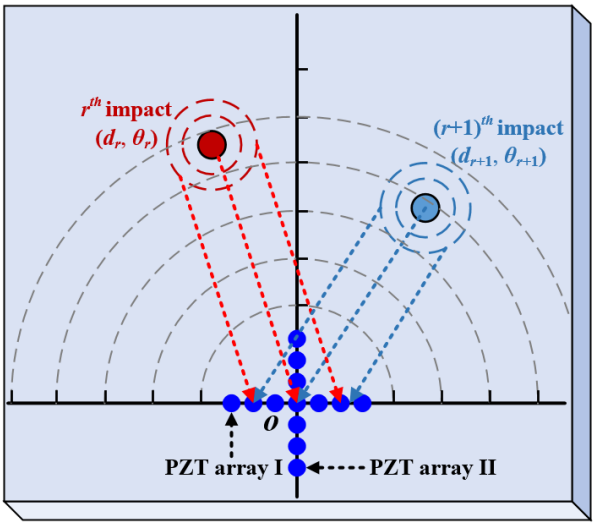

Fig. 3 The PZT 2D cross-shaped array

$$\mathbf{s}=\begin{bmatrix} \boldsymbol{s}(\rho,t_0) \\ \boldsymbol{s}(\rho,t_1) \\ \vdots \\ \boldsymbol{s}(\rho,t_T) \end{bmatrix}_{(T+1)\times M} \xrightarrow{\otimes \boldsymbol{\phi}(\rho,\xi_n)^T} \mathbf{H}=\begin{bmatrix} \boldsymbol{H}(t_0,\xi_n) \\ \boldsymbol{H}(t_1,\xi_n) \\ \vdots \\ \boldsymbol{H}(t_T,\xi_n) \end{bmatrix}_{(T+1)\times N}$$

Fig. 4 Illustration of wavenumber-time imaging process

With the PZT 2D cross-shaped array, two wavenumber-time images of PZT array I and II can be obtained respectively. The wavenumber-time image is represented as a speckle image. The abscissa of the image is wavenumber which is from $-\xi_{max}$ to ξ_{max} and the ordinate of the image is time which is from 0 to T. The normalized pixel value of each point in the wavenumber-time image represents the magnitude of the filtered output at a specific wavenumber and time point. Fig. 5 gives out the two wavenumber-time images of PZT array I and II of a dual-impact event as an example. It can be seen that every wavenumber-time image has two speckles, corresponding to the two impacts of the dual-impact event. The speckle contains the information of the impact's projection wavenumber and the absolute Time-of-Flight (ToF).

When a multi-impact event occurs, there should exist multiple speckles with corresponding projection wavenumbers and ToFs of different impacts in the wavenumber-time image. Based on these information, the localization of a single impact can be easily realized in the authors' previous study [36]. However, it is not available for the multi-impact event, because it is hard to recognize the one-to-one relationship between the two speckles of the same impact in the two wavenumber-time images, since the speckles of different impacts may have the same ToF. Besides, due to the relative positions of the multiple impacts, the speckles of different impacts may be coincident. For example, when two impacts are symmetrical about PZT array II,

their speckles in the wavenumber-time image of PZT array II will have the same ToF and projection wavenumber, resulting in coincidence of the two speckles.

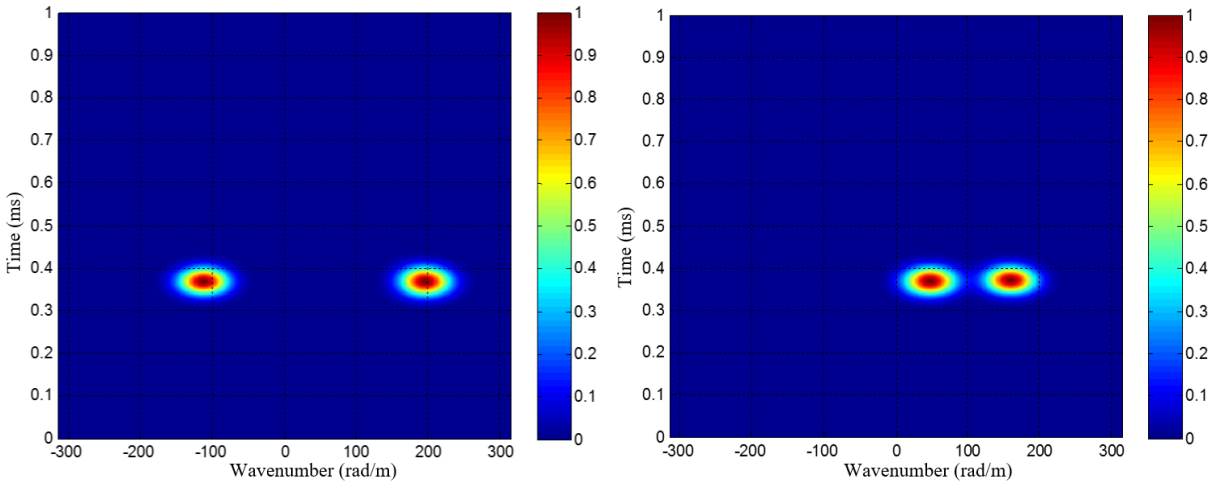

（a）Wavenumber-time image of PZT array I　　（b）Wavenumber-time image of PZT array II

Fig. 5 The sample wavenumber-time imaging result of a dual-impact event

In order to address the issues mentioned above and realize the multi-impact localization, a feature identification method of multiple impacts and an image mapping method are developed, in which the latter is able to convert the wavenumber-time image to angle-distance image based on the former's identification result. The basic principles of the methods are described as follows.

(1) Aiming at solving the one-to-one correspondence and coincident issues, the feature identification method first estimates the number of impacts R based on eigenvalue decomposition of the multi-impact signal [22, 41], then calculates the wavenumber ξ_c through a moving wavenumber window.

(2) The wavenumber ξ_c based image mapping method is proposed to realize the multi-impact localization, this method is composed of two steps, including the first step of mapping the wavenumber-time image to an angle-time image, and the second step of mapping the angle-time image to the final angle-distance image.

3.2 Feature identification method of multiple impacts

The covariance matrix of the multi-impact signal acquired by a linear PZT array can be expressed as Eq. (18). Since the multi-impact signal and the sampling noise are independent, and the signals of different impacts are also independent with each other, the eigenvalues of the covariance matrix can be calculated by performing the eigenvalue decomposition. The obtained eigenvalues in descending order are given in Eq. (19). If there are R impacts, there should be R large eigenvalues and M-R small eigenvalues. By counting the number of large eigenvalues, the number of impacts can be estimated.

$$\mathbf{S} = \frac{1}{M}\left[\mathbf{s}^T\mathbf{s}\right] \tag{18}$$

$$\lambda_1 \geq \lambda_2 \geq \cdots \geq \lambda_R > \lambda_{R+1} = \lambda_{R+2} = \cdots = \lambda_M \tag{19}$$

However, due to the limited sampling length of PZT array and the noisy nature, the eigenvalues appear as Eq. (20), resulting in that it is unable to distinguish the big eigenvalues.

$$\lambda_1 \geq \lambda_2 \geq \cdots \geq \lambda_R \geq \lambda_{R+1} \geq \lambda_{R+2} \geq \cdots \geq \lambda_M \tag{20}$$

With the PZT 2D cross-shaped array, this issue can be solved by combining the eigenvalues of PZT array I and II to get a combined group of eigenvalues to enhance the reliability, as shown in Eq. (21).

$$\lambda_i = \sqrt{\lambda_{i-\mathrm{I}}^2 + \lambda_{i-\mathrm{II}}^2} \tag{21}$$

Where $\lambda_{i\text{-}I}$ and $\lambda_{i\text{-}II}$ represent the i^{th} eigenvalue in descending order of PZT array I and II respectively.

Based on the combined eigenvalues, the big and small eigenvalues can be distinguished by setting a threshold λ_T. According to statistical analysis of numbers of multi-impact experiments, λ_T is given by Eq. (22). If an eigenvalue is bigger than λ_T, then it is regarded as a large one. There should be R eigenvalues in line with this condition when R impacts exist. Thus, the number of impacts can be estimated.

$$\lambda_T = 0.1\lambda_1 \tag{22}$$

With the number of impacts R, the wavenumber of the multi-impact signal can be calculated. Taking the r^{th} impact as an example, its two projection wavenumbers on PZT array I and II, which are denoted as ξ_r^I and ξ_r^{II}, are expressed as Eq. (23).

$$\begin{cases} \xi_r^I = \xi_c \cdot \cos\theta_r \\ \xi_r^{II} = \xi_c \cdot \cos\left(90^\circ - \theta_r\right) = \xi_c \cdot \sin\theta_r \end{cases} \tag{23}$$

It can be seen that the projection wavenumbers on PZT array I and II represent the cosine and sine values of ξ_c respectively. As discussed in Section 2.1, considering that the multi-impact signal is frequency narrow-band signal with a selected central frequency ω_c, the wavenumbers of different impacts should be the same and equal to ξ_c. According to Eq. (23), ξ_c can be expressed as Eq. (24).

$$\xi_c = \sqrt{\left(\xi_1^I\right)^2 + \left(\xi_1^{II}\right)^2} = \cdots = \sqrt{\left(\xi_r^I\right)^2 + \left(\xi_r^{II}\right)^2} = \cdots = \sqrt{\left(\xi_R^I\right)^2 + \left(\xi_R^{II}\right)^2} \tag{24}$$

For a single impact event (R=1), the wavenumber ξ_c can be easily calculated according to Eq. (24). However, it is not available for the multi-impact event, because of the one-to-one correspondence and coincident issues proposed in Section 3.1. To solve these issues and calculate ξ_c, a moving wavenumber

window is designed.

Assuming the wavenumber-time image of PZT array I has P speckles and the image of PZT array II has Q speckles, then a wavenumber matrix $\mathbf{U}$ with the size of $P\times Q$ can be built by searching all the projection wavenumbers of the two images, as shown in Eq. (25). Normally, each wavenumber-time image has R speckles, corresponding to the R impacts, namely $P=Q=R$. The wavenumber ξ_c can be obtained by searching $\mathbf{U}$ for R equal elements, denoted as ξ_1 to ξ_R, according to Eq. (24). However, limited by the resolution of the scanning spatial-wavenumber filter, the R elements may have a small deviation among each other and are only approximately equal to ξ_c. Thus a moving wavenumber window with a preset bandwidth ξ_b is designed to scan all the elements in $\mathbf{U}$ from small to large. The R close elements which are all within the window are taken to calculate ξ_c, given by Eq. (26).

$$\mathbf{U}=\begin{bmatrix} \sqrt{\left(\xi_1^I\right)^2+\left(\xi_1^{II}\right)^2} & \sqrt{\left(\xi_1^I\right)^2+\left(\xi_2^{II}\right)^2} & \cdots & \sqrt{\left(\xi_1^I\right)^2+\left(\xi_Q^{II}\right)^2} \\ \sqrt{\left(\xi_2^I\right)^2+\left(\xi_1^{II}\right)^2} & \sqrt{\left(\xi_2^I\right)^2+\left(\xi_2^{II}\right)^2} & \cdots & \sqrt{\left(\xi_2^I\right)^2+\left(\xi_Q^{II}\right)^2} \\ \vdots & \vdots & \ddots & \vdots \\ \sqrt{\left(\xi_P^I\right)^2+\left(\xi_1^{II}\right)^2} & \sqrt{\left(\xi_P^I\right)^2+\left(\xi_2^{II}\right)^2} & \cdots & \sqrt{\left(\xi_P^I\right)^2+\left(\xi_Q^{II}\right)^2} \end{bmatrix}_{P\times Q} \tag{25}$$

$$\xi_c=\frac{1}{R}\sum_{r=1}^{R}\xi_r,\quad \xi_1\approx\cdots\approx\xi_r\approx\cdots\approx\xi_R \tag{26}$$

Besides, due to the possible coincident of speckles of different impacts, the number of elements in $\mathbf{U}$ which are approximately equal to ξ_c may be not R. Under this situation, the group of elements which are all within the wavenumber window and have the maximum number are taken and averaged to calculate ξ_c. In this paper, the bandwidth ξ_b is set to be 5% of the maximum scanning wavenumber ξ_{max}.

Table 1 Eigenvalues and estimation results of the number of impacts

	Eigenvalue								Estimation result
	λ_1	λ_2	λ_3	λ_4	λ_5	λ_6	λ_7	λ_T	
PZT array I	879.4	173.0	18.4	3.0	1.0	0.3	0.2	17.3	3
PZT array II	662.1	69.0	10.5	2.8	0.3	0.1	0.0	66.2	2
Combined	1100.7	186.3	19.5	4.1	1.0	0.3	0.2	110.1	2

In order to further explain the feature identification method, the dual-impact event shown in Fig. 5 is taken to be analyzed here. By building covariance matrixes and performing eigenvalue decomposition, the eigenvalues of PZT array I and II and the combined eigenvalues are obtained, as shown in Table 1. Table 1 also gives out the eigenvalue threshold λ_T and the number of impacts estimated by the three groups of eigenvalues. It can be seen that the estimation result of PZT array I is wrong, and though the estimation result

of PZT array II is correct, its λ_T and λ_2 are very close. Compared with the eigenvalues of PZT array I and II, the combined eigenvalues have a higher reliability on the estimation result of the number of impacts.

As to the calculation of ξ_c, the projection wavenumbers of the four speckles in the two wavenumber-time images are -112 rad/m, 196 rad/m, 48 rad/m and 159 rad/m respectively. Then the wavenumber matrix U is obtained, as shown in Eq. (27). With the maximum scanning wavenumber of 314 rad/m, the bandwidth ξ_b of the moving wavenumber window is set to be 16 rad/m. The searching result is given out in Fig. 6, from which it can be seen that the 2 elements within the window are 194.5 rad/m and 201.8 rad/m. Hence the wavenumber of the multi-impact signal ξ_c is 198.2 rad/m, according to Eq. (26).

$$\mathbf{U}=\begin{bmatrix}121.8 & 194.5\\ 201.8 & 252.4\end{bmatrix}_{2\times 2} \tag{27}$$

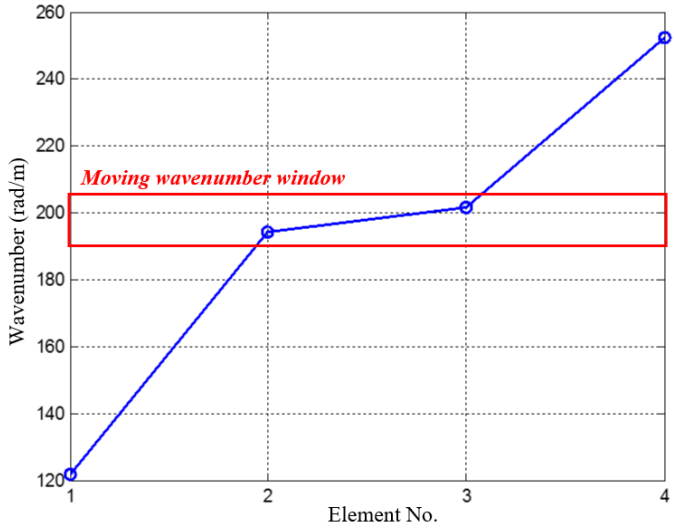

Fig. 6 Searching result of the moving wavenumber window

3.3 Image mapping method from wavenumber-time image to angle-distance image

In Section 3.1, the method of wavenumber-time imaging is given but it cannot be used to realize the multi-impact localization directly. Thus, a simple mapping method is proposed to convert the wavenumber-time image to angle-time image, and then to angle-distance image, in which the polar coordinates of multiple impacts can be obtained.

The schematic diagram of the conversion from wavenumber-time image to angle-time image is given out in Fig. 7. Every pixel point in the angle-time image stands for a possible impact source with its own angle and ToF. Selecting a point (t, θ) in the angle-time image optionally, its two projection points in the wavenumber-time images of PZT array I and II are (t, $\xi_c \cdot cos\theta$) and (t, $\xi_c \cdot sin\theta$), according to Eq. (23). Then its pixel value $\mathbf{G}(t, \theta)$ can be calculated by summing the pixel values of the two projection points, defined as Eq.

(28). The larger its pixel value is, the more likely it can be considered as an actual impact source.

$$\mathbf{G}(t,\theta)=\mathbf{H}^{\mathbf{I}}(t,\xi_c\cdot\cos\theta)+\mathbf{H}^{\mathbf{II}}(t,\xi_c\cdot\sin\theta) \tag{28}$$

Where **G** represents the angle-time image, $\mathbf{H}^{\mathbf{I}}$ and $\mathbf{H}^{\mathbf{II}}$ represent the wavenumber-time images of PZT array I and II respectively. Repeating this process and calculating the pixel values of all the points, the angle-time image is achieved.

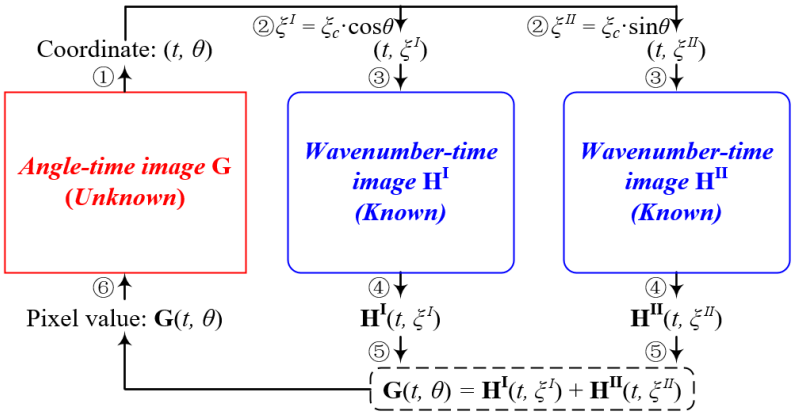

Fig. 7. The conversion from wavenumber-time image to angle-time image

In the process of converting the angle-time image to angle-distance image, the impact occurring time is necessary, since the ToF in the angle-time image is not the actual impact propagation time and cannot be used to estimate the impact distance. Hence, besides the proposed frequency ω_c, another different frequency is introduced to calculate the impact occurring time and generate the angle-distance image. Denoting the group velocities of the two central frequencies as v_{g1} and v_{g2}, the ToFs of the r^{th} impact under the two frequencies as t_{r1} and t_{r2}, then the occurring time of the r^{th} impact t_{re} can be calculated, expressed as Eq. (29) and (30).

$$t_{re}=t_{r1}-\frac{d_r}{v_{g1}}=t_{r2}-\frac{d_r}{v_{g2}} \tag{29}$$

$$t_{re}=\frac{v_{g1}\cdot t_{r1}-t_{r2}\cdot v_{g2}}{v_{g1}-v_{g2}} \tag{30}$$

Considering that the multiple impacts occur at the same time, they should have the same occurring time. Thus a more accurate impact occurring time t_e is obtained by averaging the t_{re} values of all the R impacts.

$$t_e=\frac{1}{R}\cdot\sum_{r=1}^{R}t_{re} \tag{31}$$

With the impact occurring time t_e, the angle-distance image can be achieved, which is similar to the angle-time imaging, as shown in Fig. 8. Selecting a point $(d,\ \theta)$ in the angle-distance image optionally, its two projection points in the two angle-time images are $(d/v_{g1}+t_e,\ \theta)$ and $(d/v_{g2}+t_e,\ \theta)$, according to Eq. (29). And

its pixel value can be calculated by summing the pixel values of the two projection points.

$$\mathbf{E}(d,\theta)=\mathbf{G}(d/v_{g1}+t_e,\theta)+\mathbf{G}'(d/v_{g2}+t_e,\theta) \tag{32}$$

Where **E** represents the angle-distance image, **G** and **G′** represent the angle-time images under different frequencies. Repeating this process and calculating the pixel values of all the points, the angle-distance image is achieved. According to the number of impacts *R* estimated before, the polar coordinates of the impacts can be directly obtained.

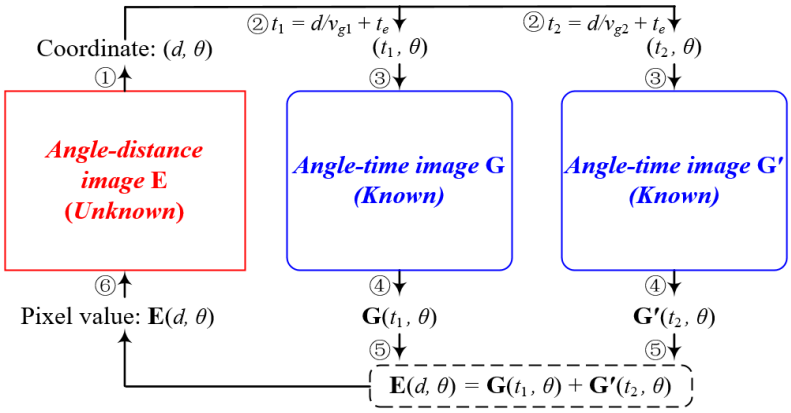

Fig. 8. The conversion from angle-time image to angle-distance image

3.4 The overall architecture of the multi-impact imaging and localization method

According to the research mentioned above, the implementation process of the multi-impact imaging and localization method is summarized as Fig. 9, which mainly consists of the following parts.

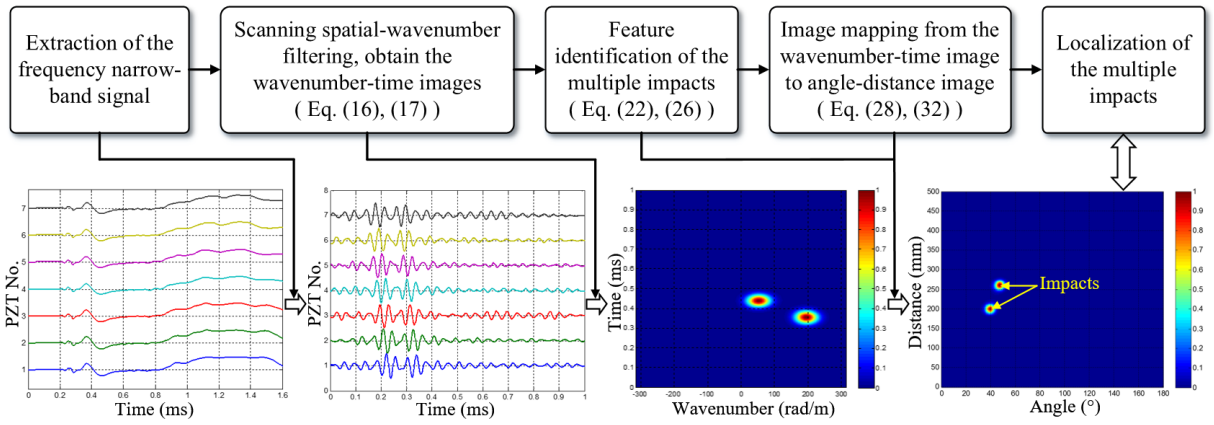

Fig. 9. The overall architecture of the multi-impact imaging and localization method

(1) Extraction of the frequency narrow-band signal.

(2) Scanning spatial-wavenumber filtering, obtain the wavenumber-time images.

(3) Feature identification of the multiple impacts, including estimation of the number of impacts and the wavenumber of the multi-impact signal.

(4) Image mapping from the wavenumber-time image to angle-distance image.

(5) Localization of the multiple impacts, through directly obtaining their polar coordinates from the angle-distance image.

4. Validation of the multi-impact imaging and localization method

4.1 Validation setup

The validation system is shown in Fig. 10(a). A carbon fiber laminate plate is adopted, which has the dimension of 600 mm × 600 mm × 2.5 mm (Length × Width × Thickness) and consists of 18 stacked layers. The thickness of each layer is 0.125 mm and the ply sequence is $[45/0/-45/90/0/-45/0/-45/0]_s$. The material property of a single layer is given in Table 2. The 4 sides of the plate are fixed between 2 fixtures by a series of bolts. Supported by the bolts, the plate and the fixtures are placed on a table horizontally, and do not directly contact the table.

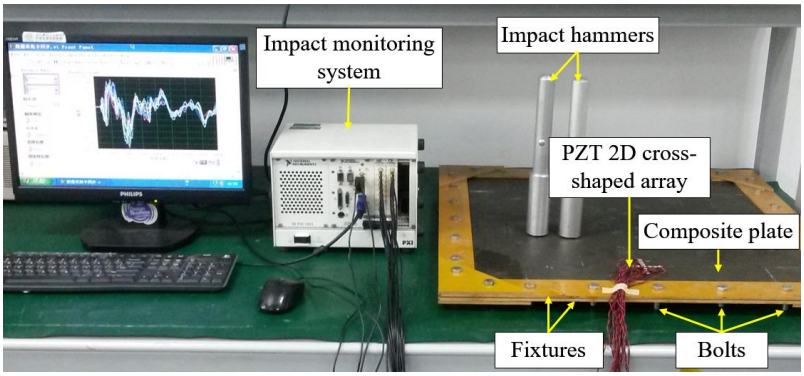

（a）Validation system

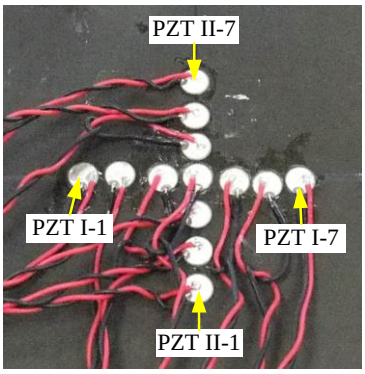

（b）PZT 2D cross-shaped array

Fig. 10 The validation system of the multi-impact imaging method

Table 2 The material property of a single layer of the composite plate

Parameter	Value
0º tensile modulus (GPa)	135
90º tensile modulus (GPa)	8.8
±45º in-plane shearing modulus (GPa)	4.47
Poisson ratio μ	0.328
Density ($kg \cdot m^{-3}$)	1.61×10^3

A PZT 2D cross-shaped array shown in Fig. 10(b) is attached to the structure, each linear array contains 7 PZT sensors with a diameter of 8 mm and a thickness of 0.48 mm. The interval between every two adjacent PZT sensors is τ=10 mm. The PZTs in PZT array I are labeled as PZT I-1, PZT I-2, …, PZT I-7 and those in PZT array II are labeled as PZT II-1, PZT II-2, …, PZT II-7. PZT I-4 and PZT II-4 are the same one.

In this paper, the validation focuses on dual-impact events. Two same impact hammers are adopted to apply impacts to the structure. As shown in Fig. 11, the impact hammer mainly consists of a trigger, an inside

spring and a copper block connected to it. With the impact hammer, the impact can be applied to the structure according to the following steps.

(1) Compressing and locking the spring by pushing the copper block.

(2) Placing the impact hammer on the structure vertically.

(3) Pressing the trigger and ejecting the copper block to hit the structure.

The mass and diameter of the copper block is 25 g and 20 mm, respectively. Depending on the compression degree of the spring, there are 4 energy levels of the impact hammer, as shown in Table 3. Level I with the energy of 0.21 J is used in this paper. The corresponding velocity of the copper block is about 4 m/s. By pressing the triggers of the two impact hammers simultaneously, having two impacts at the same time can be realized approximately.

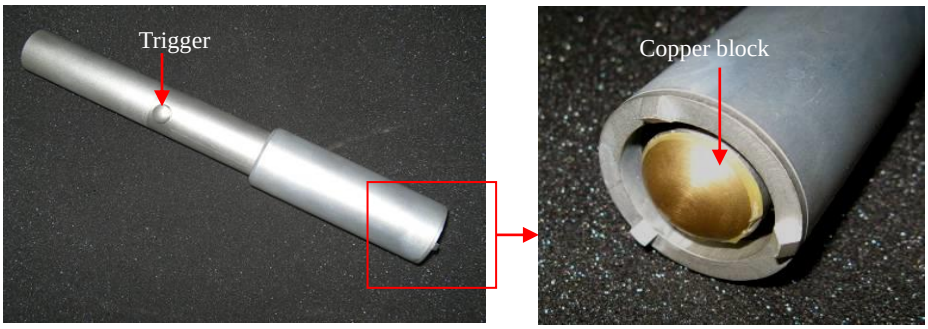

Fig. 11 The impact hammer

Table 3 The 4 energy levels of the impact hammer

Level	I	II	III	IV
Energy (J)	0.21	0.62	1.31	2.48

Besides, an impact monitoring system is adopted to acquire impact response signals of the 13 PZTs synchronously. Based on the National Instruments (NI) PXI-1031 chassis, the system integrates two NI PXI-5105 data acquisition boards with a total of 16 channels. A LabVIEW platform based monitoring software working in the system is designed to control the data acquisition and storage. The sampling rate is set to be 2 MS/s, and the sampling length is 10000 samples, including 1000 pre-trigger samples. The trigger channel is set to be PZT I-1 with a trigger voltage of 2 V. For each multi-impact event in the validation, about 6 measurements are taken and used to conduct multi-impact localization. Since the localization results are usually very close, only a representative result is given out in the validation.

Taking the center of PZT I-4/ II-4 as the pole, a polar coordinate system is built. A total of ten dual-impact events which are divided into two cases are performed, as shown in Table 4 and Fig. 12. Table 4 gives out the polar coordinates of the impacts. In Fig. 12, two impacts with the same number belong to one

dual-impact event. What should be noted is that some impacts belong to multiple dual-impact events. The 2 cases of dual-impact events are explained as follows.

Table 4 Polar coordinates of the 10 dual-impact events

Case No.	Dual-impact No.	Dual-impact position (mm, °)	
		Impact 1	Impact 2
1	1	(150, 90)	(200, 90)
	2	(150, 120)	(200, 10)
	3	(200, 40)	(250, 40)
	4	(200, 30)	(250, 50)
	5	(150, 10)	(200, 0)
	6	(150, 100)	(200, 110)
	7	(200, 130)	(250, 90)
	8	(150, 10)	(150, 90)
2	9	(200, 80)	(200, 100)
	10	(250, 40)	(250, 140)

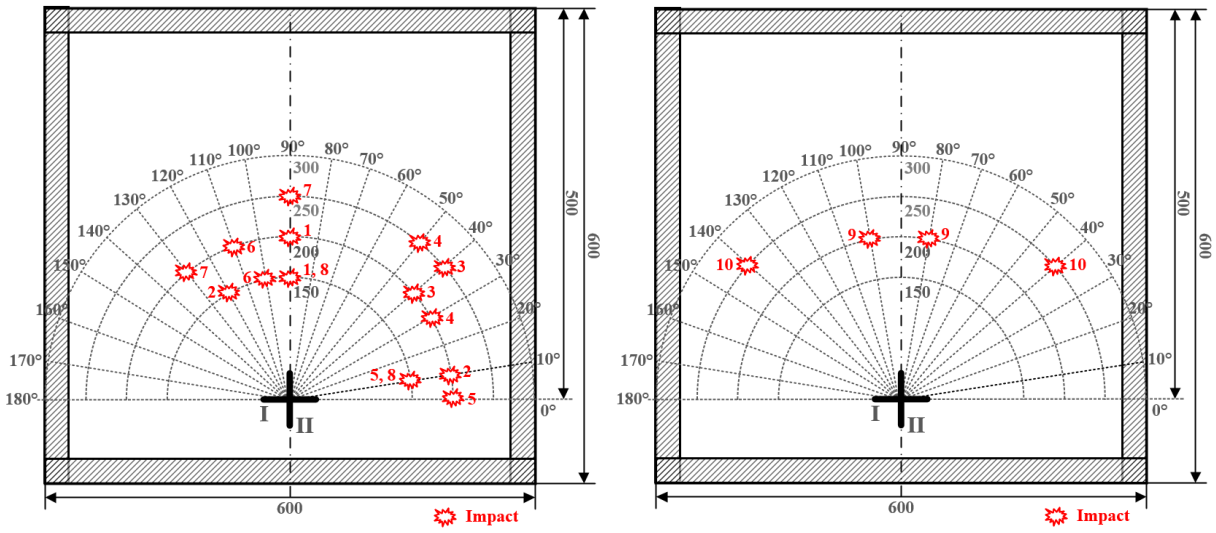

（a）Dual-impact positions of case 1　　（b）Dual-impact positions of case 2

Fig. 12 Dual-impact positions of the 2 proposed cases

Case 1: Normal situation, different speckles of different impacts in the wavenumber-time are separated. In particular, some dual-impact events (No. 1, 5, 7 and 8) have angles like 0° and 90°, which are conventional blind angles to PZT array I and PZT array II respectively.

Case 2: Coincident situation, as mentioned in Section 3.1, when two impacts are symmetrical about PZT array II, the speckles of them are coincident in the wavenumber-time image of PZT array II.

4.2 Multi-impact signal and wavenumber-time imaging

The 1st dual-impact event listed in Table 3 is chosen as an example to be analyzed here. The positions of the two impacts are (150 mm, 90°) and (200 mm, 90°). Fig. 13 gives out the frequency wideband response

signals of PZT array I and II. Fig. 14 shows the frequency spectrum of PZT I-4/II-4. It can be seen that the main energy of the signal is within the frequency band from 0 Hz to 50 kHz.

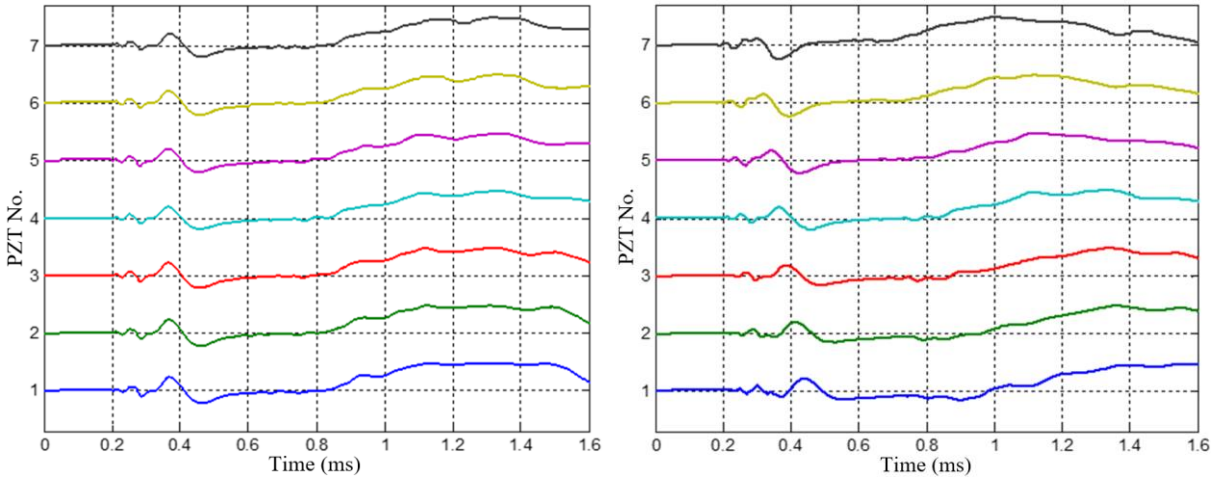

（a）Frequency wideband response signals of PZT array I　　（b）Frequency wideband response signals of PZT array II

Fig. 13 The frequency wideband response signals of the 1st dual-impact

As mentioned in Section 3.3, the multi-impact signals of two different central frequencies ω_1 and ω_2 (ω_2 is larger than ω_1) are needed to achieve angle-distance imaging. In order to guarantee an accurate impact localization, the selection of the two frequencies should consider the following aspects.

(1) The two frequencies ω_1 and ω_2 should be within 0~50 kHz, considering the energy distribution.

(2) The difference between ω_1 and ω_2 should be large enough, since the larger the difference is, the bigger the corresponding group velocity contrast will be. According to Eq. (30), this is helpful to reduce the calculation error of the impact occurring time.

(3) The wavenumber corresponding to the high frequency ω_2 should be less than the maximum scanning wavenumber ξ_{max} decided by the spatial sampling rate.

(4) As to the low frequency ω_1, if it is too small, the time domain resolution will be too low to identify the arrival time. Besides, the low resolution may also result in the overlap of speckles of different impacts in the wavenumber-time image.

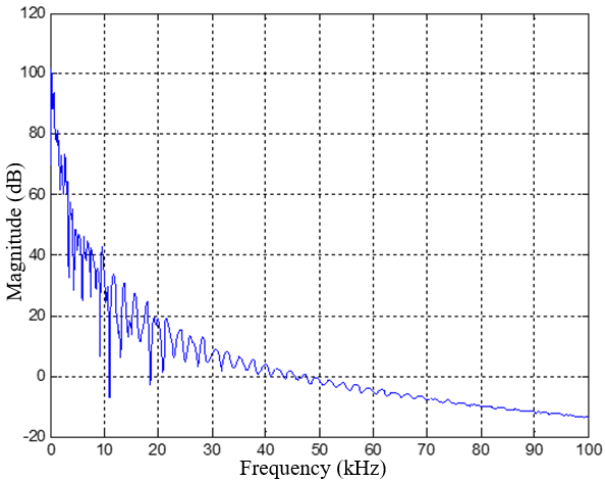

Fig. 14 Frequency spectrum of the response signal of PZT I-4/II-4

According to the above discussion, ω_1 and ω_2 are set to be 20 kHz and 35 kHz respectively. Fig. 15 and Fig. 16 give out the extracted frequency narrow-band signals of the two frequencies, namely the multi-impact signals. It can be found that the signals of the two impacts are mixed in Fig. 15, due to the low frequency and time domain resolution, but the signals in Fig. 16 are obviously separated.

Since τ=10 mm, the maximum scanning wavenumber of the scanning spatial-wavenumber filter is ξ_{max}=314 rad/m, according to Eq. (14). After conducting the scanning spatial-wavenumber filtering on the multi-impact signals shown in Fig. 15 and 16, the wavenumber-time images of PZT array I and II of 20 kHz and 35 kHz are obtained, as shown in Fig. 17(a)~(d). Two speckles can be recognized in each of the wavenumber-time images.

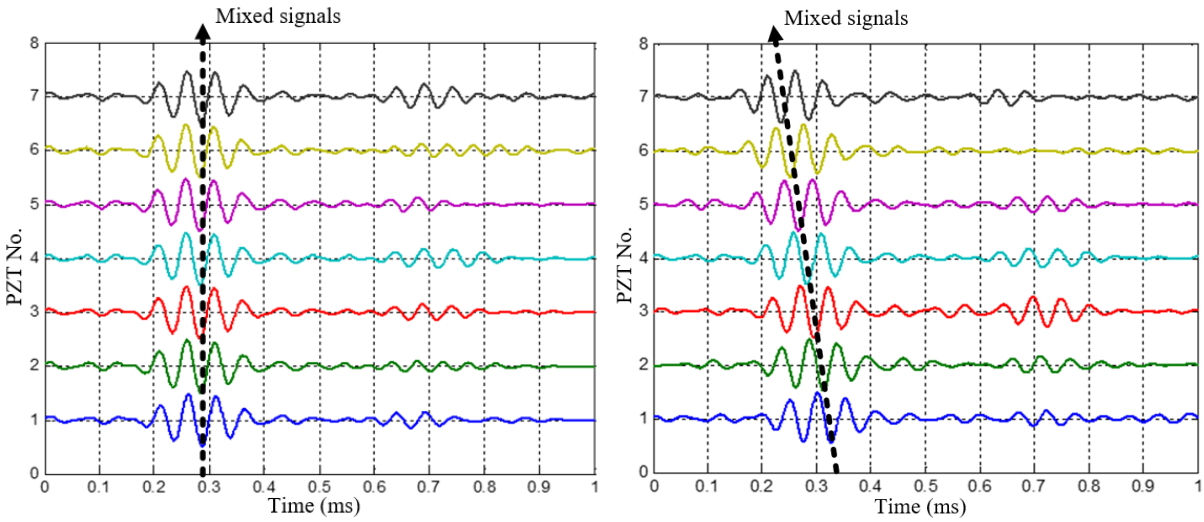

（a）Frequency narrow-band signals of PZT array I　　（b）Frequency narrow-band signals of PZT array II

Fig. 15 The extracted frequency narrow-band signals of 20 kHz of the 1st dual-impact event

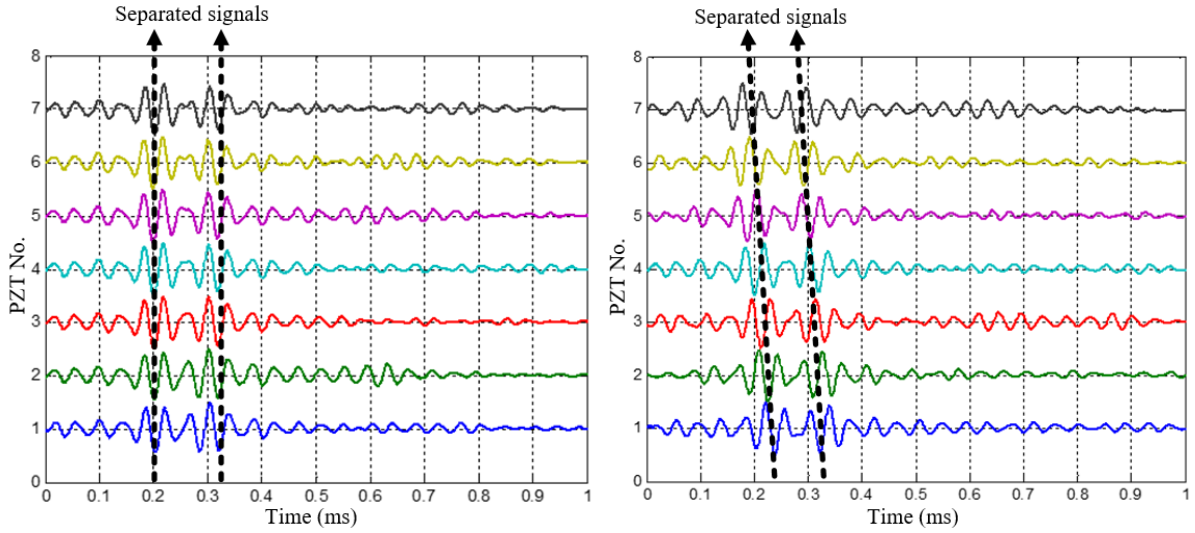

（a）Frequency narrow-band signals of PZT array I　（b）Frequency narrow-band signals of PZT array II

Fig. 16 The extracted frequency narrow-band signals of 35 kHz of the 1st dual-impact event

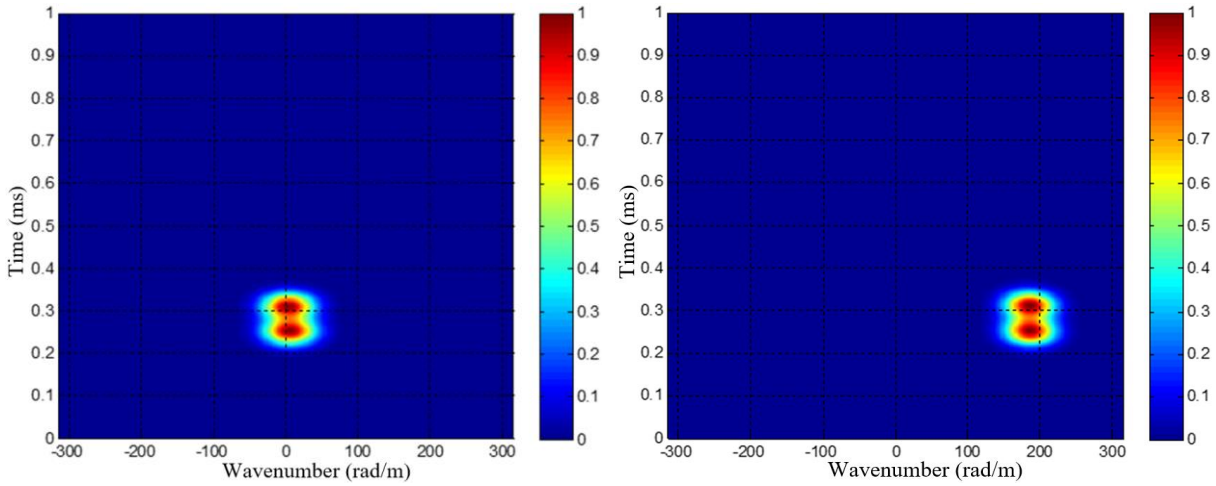

（a）Wavenumber-time image of PZT array I of 20 kHz　（b）Wavenumber-time image of PZT array II of 20 kHz

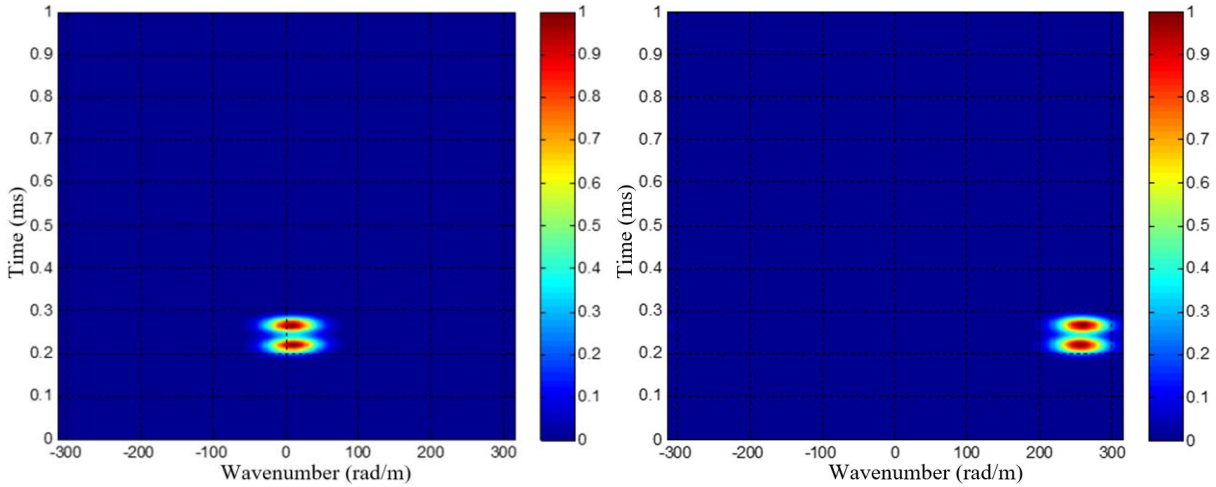

（c）Wavenumber-time image of PZT array I of 35 kHz　（d）Wavenumber-time image of PZT array II of 35 kHz

Fig. 17 The wavenumber-time images of the 1st dual-impact event

4.3 Multi-impact feature identification and the image mapping

With the frequency narrow-band signals, the corresponding covariance matrixes and eigenvalues can be calculated, then the combined eigenvalues are also available, as shown in Table 5. Based on Eq. (22), the threshold value λ_T of the 1st dual-impact event is 85.3, which is between λ_2 and λ_3, so the estimation result of the number of impacts is 2. Table 5 also lists the estimation results of the other 9 dual-impact events, which are all correct.

Table 5 Eigenvalues distribution and estimation results of the number of impacts

Dual-impact No.	Eigenvalue								Estimation result
	λ_1	λ_2	λ_3	λ_4	λ_5	λ_6	λ_7	λ_T	
1	853.3	197.3	20.9	8.9	1.4	0.5	0.2	85.3	2
2	721.1	176.9	23.8	7.7	1.1	0.3	0.3	72.1	2
3	314.8	77.1	13.0	2.5	0.3	0.0	0.0	31.5	2
4	341.9	98.4	21.1	2.4	0.6	0.1	0.1	34.2	2
5	849.9	197.3	24.4	8.1	1.4	0.4	0.4	85.0	2
6	912.4	197.3	14.3	6.9	1.5	0.5	0.2	91.2	2
7	766.1	137.8	15.2	4.3	0.7	0.1	0.1	76.6	2
8	1913.3	372.8	25.4	6.7	1.2	0.4	0.2	191.3	2
9	2047.9	487.2	29.7	5.0	1.1	0.2	0.1	204.8	2
10	583.3	150.8	11.5	1.8	0.3	0.0	0.0	58.3	2

Based on Fig. 17, the wavenumber ξ_c of the 1st dual-impact event can be calculated. In Fig. 17(a), the projection wavenumbers and ToFs of the impacts are (0.3065 ms, 4 rad/m) and (0.2545 ms, 6 rad/m), and they are (0.3090 ms, 186 rad/m) and (0.2545 ms, 186 rad/m) in Fig. 16(b). With the maximum scanning wavenumber of ξ_{max}=314 rad/m, the wavenumber window bandwidth ξ_b is set to be 16 rad/m. Then the wavenumber of the multi-impact signal of 20 kHz can be calculated, which is 186 rad/m. Similarly, the wavenumber of 35 kHz is calculated as 258 rad/m.

With the wavenumbers of the multi-impact signals of the two frequencies, Fig. 17(a) and (b) can be mapped to the angle-time image of 20 kHz, Fig. 17(c) and (d) can be mapped to the angle-time image of 35 kHz, as shown in Fig. 18(a) and (b). In order to convert the angle-time image to angle-distance image, the group velocities of the two frequencies are needed. In this paper, the group velocity is obtained through measuring and averaging the group velocities of the modulated five-cycle sine burst signals excited in the composite plate of different directions [36]. The average group velocities of 20 kHz and 35 kHz are v_{g1} =1152.6 m/s and v_{g2} =1429.2 m/s respectively. Fig. 18(c) gives out the final angle-distance image. Then the polar coordinates of the 1st dual-impact event are obtained, which are (161.5 mm, 88.1°) and (181.7 mm, 88.8°). The green circles in Fig. 18(c) represent the actual positions of the two impacts for reference. The

localization error of the first impact is 12.6 mm, and the second is 18.7 mm.

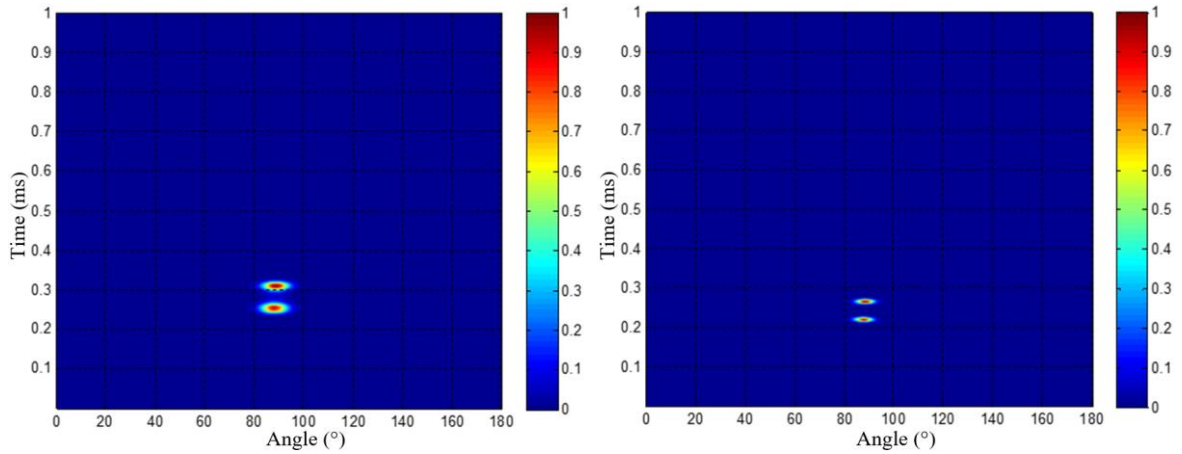

（a）Angle-time image of 20kHz

（b）Angle-time image of 35kHz

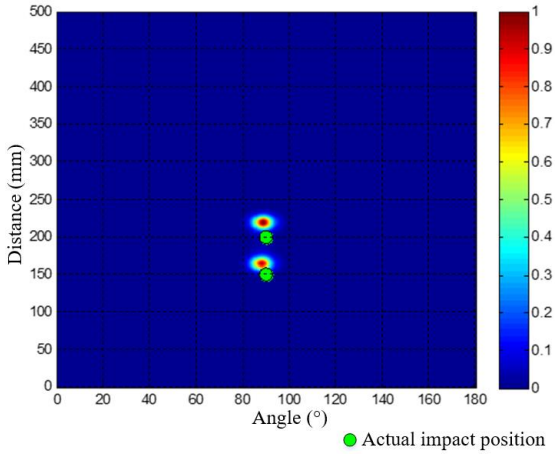

（c）Final angle-distance image

Fig. 18 Imaging and localization result of the 1st dual-impact event

4.4 Multi-impact localization results

In Section 4.2 and 4.3, the 1st dual-impact event belonging to Case 1 is taken as an example to verify the proposed multi-impact imaging and localization method. In addition, the localization result of the 9th dual-impact event which belongs to Case 2 is also given out to verify the method's ability of solving the coincident issue, as shown in Fig. 19. The two impacts of the 9th dual-impact event are symmetrical about PZT array II. Fig. 19(a) and (b) show the two wavenumber-time images of PZT array I and II of 20 kHz, the former one has two speckles with the projection wavenumbers of -38 rad/m and 52 rad/m respectively, and the latter one only has one speckle with the projection wavenumber of 183 rad/m, because of the coincident issue. With the proposed feature identification method, the wavenumber ξ_c of 20 kHz is calculated as 189 rad/m. The two wavenumber-time images of 35 kHz have the similar speckle distribution, as shown in Fig. 19(c) and (d), and the wavenumber ξ_c is 261 rad/m. Fig. 19(e) gives out the final angle-distance image of the

9th dual-impact event, it can be seen that the method is able to distinguish and locate the multiple impacts, though the speckles of different impacts are coincident in the wavenumber-time image of PZT array II.

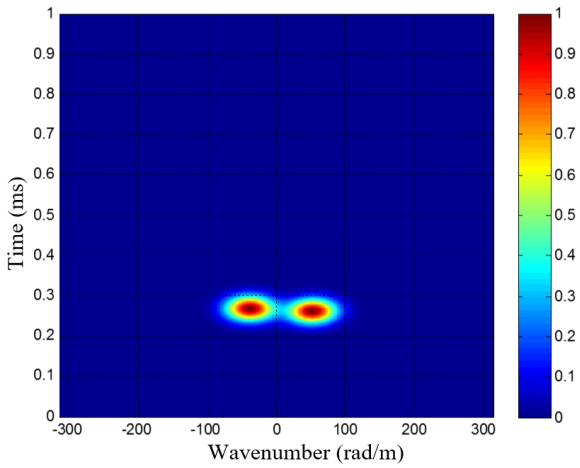

（a）Wavenumber-time image of PZT array I of 20 kHz

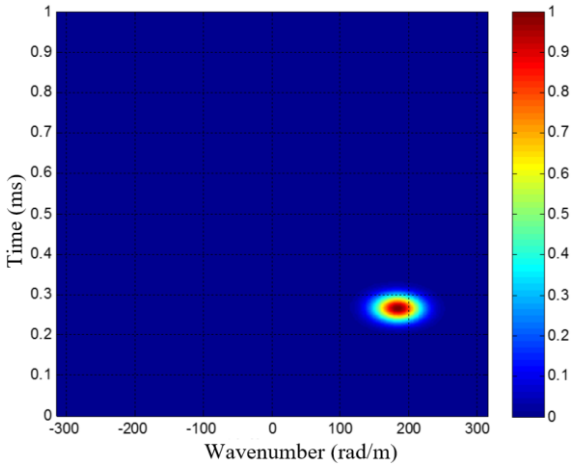

（b）Wavenumber-time image of PZT array II of 20 kHz

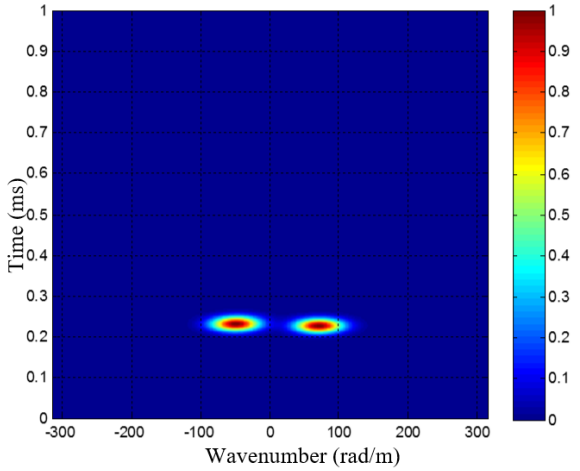

（c）Wavenumber-time image of PZT array I of 35 kHz

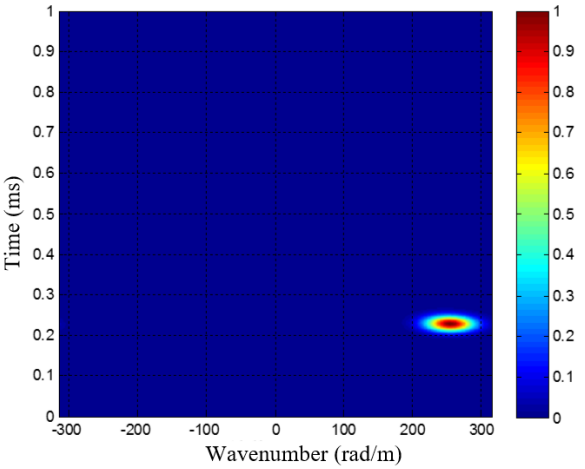

（d）Wavenumber-time image of PZT array II of 35 kHz

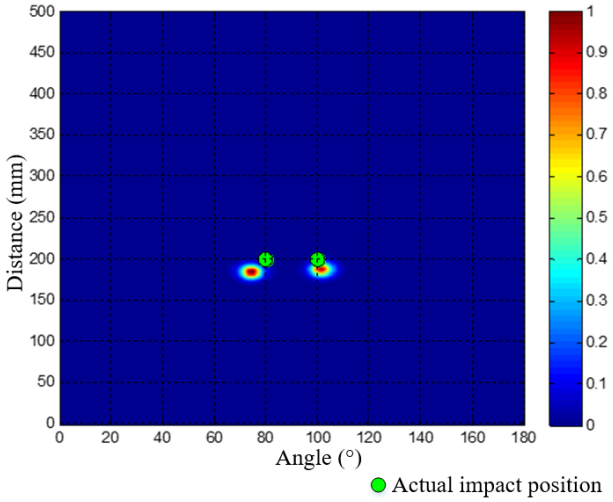

（e）Final angle-distance image

Fig. 19 Imaging and localization result of the 9th dual-impact

Based on the locating process mentioned above, the localization results of all the 10 dual-impact events of the 2 cases are obtained and listed in Table 6, all the dual-impact events are in good agreement with their actual positions. The maximum localization error is about 2 cm, and there is no significant difference between the localization results of the 2 cases. In addition, the 1st, 5th, 7th and 8th dual-impact events, which have conventional blind angels 0° and 90° mentioned in Section 4.1, are also correctly located. In summary, the statistical results have proved the effectiveness of the presented methods.

Table 6 Statistical localization results of the 10 dual-impact events

No.	Impact 1				Impact 2			
	Actual position (mm, °)	Localization result (mm, °)	Error		Actual position (mm, °)	Localization result (mm, °)	Error	
			Distance and angle (mm, °)	Position (mm)			Distance and angle (mm, °)	Position (mm)
1	(150, 90)	(161.5, 88.1)	(11.5, 1.9)	12.6	(200, 90)	(181.7, 88.8)	(18.3, 1.2)	18.7
2	(150, 120)	(151.2, 123.4)	(1.2, 3.4)	9.0	(200, 10)	(208.2, 11.2)	(8.2, 1.2)	9.3
3	(200, 40)	(200.6, 39.6)	(0.6, 0.4)	1.6	(250, 40)	(247.3, 39.1)	(2.7, 0.9)	4.7
4	(200, 30)	(193.1, 31.4)	(6.9, 1.4)	8.5	(250, 50)	(265, 47.5)	(15, 2.5)	18.8
5	(150, 10)	(168.1, 12.5)	(18.1, 2.5)	19.4	(200, 0)	(208.2, 0.2)	(8.2, 0.2)	8.3
6	(150, 100)	(151.4, 101.3)	(1.4, 1.3)	3.7	(200, 110)	(199.4, 114.6)	(0.6, 4.6)	16.1
7	(200, 130)	(214.5, 133.8)	(14.5, 3.8)	20.0	(250, 90)	(266.3, 88.6)	(16.3, 1.4)	17.5
8	(150, 10)	(165.8, 8.6)	(15.8, 1.4)	16.3	(150, 90)	(163.4, 87.3)	(13.4, 2.7)	15.3
9	(200, 80)	(183, 74.4)	(17, 5.6)	25.4	(200, 100)	(194.3, 101.3)	(5.7, 1.3)	7.3
10	(250, 40)	(245.2, 38.3)	(4.8, 1.7)	8.8	(250, 140)	(271, 141)	(21, 1)	21.8

5. Conclusions

Aiming at applying the technique of spatial-wavenumber filter to on-line multi-impact monitoring, this paper proposes a new multi-impact imaging method based on a scanning spatial-wavenumber filter which can be applied to aircraft composite structure without wavenumber measuring or modeling. Combining with the multi-impact feature identification method and the image mapping method, the multiple impacts can be imaged and located without blind angle. The validation performed on the carbon fiber laminate plate shows the effectiveness of the proposed methods. However, there still exist some issues that need to be addressed in the future work.

(1) The imaging precision should be improved before it can be applied to complex composite structures. This can be realized by improving the proposed method and eliminating the dependence on wave velocity.

(2) The method proposed in this paper is in the far-field assumption. Considering the situation that impact occurs in near-field, thus a spatial-wavenumber filter based full-field multi-impact imaging method should be developed.

(3) By increasing the sensor number of the PZT 2D cross-shaped array and reducing the distance

between two adjacent PZTs, the wavenumber directivity can be enhanced and the spatial sampling rate can be improved as well.

(4) During the localization process, the frequency narrow-band signal is extracted to realize the one-to-one relationship between the wavenumber of the signal and its propagating direction, resulting in that it's hard to be used to estimate the accurate impact energy directly. In the ongoing research, the method of estimating the energy level of impact by combining the strength of the extracted signal and the information given by the angle-distance image will be studied, which is helpful to further improve the method proposed in this paper and instruct damage inspection for aircraft composite structures.

(5) The current selection method of the threshold λ_T is based on statistical analysis, and should be further optimized to be a more easily applicable method and to ensure the reliability of estimating the number of impacts.

Acknowledgements

This work is supported by the National Natural Science Funds for Distinguished Young Scholars (Grant No.51225502), the Key Program of National Natural Science Foundation (Grant No.51635008), the Aviation Foundation (Grant No. 20140952010), State Key Laboratory of Mechanics and Control of Mechanical Structures (Grant No. 0515Y01), the Fundamental Research Funds for the Central Universities (Grant No. NE2016001), the Hong Kong Scholars Program, the Priority Academic Program Development of Jiangsu Higher Education Institutions, the Qing Lan and Young Elite Scientist Sponsorship Program by CAST of China.

References

[1] M. T. H. Sultan, K. Worden, S. G. Pierce, D. Hickey, W. J. Staszewski, J. M. Dulieu-Barton, A. Hodzic, On impact damage detection and quantification for CFRP laminates using structural response data only, Mech. Syst. Signal Process. 25 (2011) 3135-3152.

[2] V. Y. Senyurek, Detection of cuts and impact damage at the aircraft wing slat by using lamb wave method, Measurement 67 (2015) 10-23.

[3] Z. Su, L. Cheng, X. Wang, L. Yu, C. Zhou, Predicting delamination of composite laminates using an imaging approach, Smart Mater. Struct. 18 (2009) 074002.

[4] T. Wandowski, P. H. Malinowski, W. M. Ostachowicz, Circular sensing networks for guided waves based structural health monitoring, Mech. Syst. Signal Process. 66 (2016) 248-267.

[5] C. Boller, F. K. Chang, Y. Fujino, Encyclopedia of Structural Health Monitoring, John Wiley and Sons,

Hoboken, 2009.

[6] C. Zhou, Z. Su, L. Cheng, Probability-based diagnostic imaging using hybrid features extracted from ultrasonic Lamb wave signals, Smart Mater. Struct. 20 (2011) 125005.

[7] F. Ciampa, M. Meo, E. Barbieri, Impact localization in composite structures of arbitrary cross section, Struct. Health Monit. 11 (2012) 643-655.

[8] Z. Su, C. Zhou, M. Hong, L. Cheng, Q. Wang, X. Qing, Acousto-ultrasonics-based fatigue damage characterization: Linear versus nonlinear signal features, Mech. Syst. Signal Process. 45 (2014) 225-239.

[9] M. Meo, G. Zumpano, M. Piggott, G. Marengo, Impact identification on a sandwich plate from wave propagation responses, Compos. Struct. 71 (2005) 302-306.

[10] C. Zhou, Z. Su, L. Cheng, Quantitative evaluation of orientation-specific damage using elastic waves and probability-based diagnostic imaging, Mech. Syst. Signal Process. 25 (2011) 2135-2156.

[11] D. Wang, L. Ye, Z. Su, Y. Lu, Quantitative identification of multiple damage in laminated composite beams using A0 Lamb mode, J. Compos. Mater. 45 (2011) 2061-2069.

[12] H. Nakatani, T. Kundu, N. Takeda, Improving accuracy of acoustic source localization in anisotropic plates, Ultrasonics 54 (2014) 1776-1788.

[13] Z. Sharif-Khodaei, M. Ghajari, M. H. Aliabadi, Determination of impact location on composite stiffened panels, Smart Mater. Struct. 21 (2012) 105026.

[14] E. D. Niri, A. Farhidzadeh, S. Salamone, Nonlinear kalman filtering for acoustic emission source localization in anisotropic panels, Ultrasonics 54 (2014) 486-501.

[15] J. Park, S. Ha, F.K. Chang, Monitoring impact events using a system-identification method, AIAA J. 47 (2009) 2011-2021.

[16] C. C. Chia, J. R. Lee, C. Y. Park, Radome health management based on synthesized impact detection, laser ultrasonic spectral imaging, and wavelet-transformed ultrasonic propagation imaging methods, Compos. Pt. B-Eng. 43 (2012) 2898-2906.

[17] F. Ciampa, M. Meo, Impact detection in anisotropic materials using a time reversal approach, Struct. Health Monit. 11 (2012) 43-49.

[18] L. Qiu, S. Yuan, X. Zhang, Y. Wang, A time reversal focusing based impact imaging method and its evaluation on complex composite structures, Smart Mater. Struct. 20 (2011) 105014.

[19] B. Park, H. Sohn, S. E. Olson, M. P. DeSimio, K. S. Brown, M. M. Derriso, Impact localization in

complex structures using laser-based time reversal, Struct. Health Monit. 11 (2012) 577-588.

[20] L. Qiu, S. Yuan, A phase synthesis time reversal impact imaging method for on-line composite structure monitoring, Smart Struct. Syst. 8 (2011) 303-320.

[21] C. Chen, Y. Li, F. G. Yuan, Impact source identification in finite isotropic plates using a time-reversal method: experimental study, Smart Mater. Struct. 21 (2012) 105025.

[22] Y. Zhong, S. Yuan, L. Qiu, Multi-impact source localisation on aircraft composite structure using uniform linear PZT sensors array, Struct. Infrastruct. Eng. 11 (2015) 310-320.

[23] H. J. Yang, Y. J. Lee, S. K. Lee, Impact source localization in plate utilizing multiple signal classification, Proc. Inst. Mech. Eng. Part C-J. Mech. Eng. Sci. 227 (2013) 703-713.

[24] Y. Liu, A. Chattopadhyay, Low-velocity impact damage monitoring of a sandwich composite wing, J. Intell. Mater. Syst. Struct. 24 (2013) 2074-2083.

[25] L. H. Kang, Vibration and impact monitoring of a composite-wing model using piezoelectric paint, Adv. Compos. Mater. 23 (2014) 73-84.

[26] N. Quaegebeur, T. Padois, P. A. Gauthier, P. Masson, Enhancement of time-domain acoustic imaging based on generalized cross-correlation and spatial weighting, Mech. Syst. Signal Process. 75 (2016) 515-524.

[27] P. Kudela, M. Radzieński, W. Ostachowicz, Identification of cracks in thin-walled structures by means of wavenumber filtering, Mech. Syst. Signal Process. 50 (2015) 456-466.

[28] H. Sohn, D. Dutta, J.Y. Yang, M. DeSimio, S. Olson, E. Swenson, Automated detection of delamination and disbond from wavefield images obtained using a scanning laser vibrometer, Smart Mater. Struct. 20 (2011) 045017.

[29] P. F. Pai, M. J. Sundaresan, Space–wavenumber and time–frequency analysis for damage inspection of thin-walled structures, Struct. Health Monit. 11 (2012) 452-471.

[30] M. H. Sherafat, R. Guitel, N. Quaegebeur, P. Hubert, L. Lessard, P. Masson, Structural health monitoring of a composite skin-stringer assembly using within-the-bond strategy of guided wave propagation, Mater. Des. 90 (2016) 787-794.

[31] A. S. Purekar, D. J. Pines, Damage detection in thin composite laminates using piezoelectric phased sensor arrays and guided lamb wave interrogation, J. Intell. Mater. Syst. Struct. 21 (2010) 995-1010.

[32] Y. Wang, S. Yuan, L. Qiu, Improved wavelet-based spatial filter of damage imaging method on composite structures, Chinese J. Aeronaut. 24 (2011) 665-672.

[33] H. Y. Guo, Z. L. Li, Two-stage multi-damage detection method based on energy balance equation, J. Nondestruct. Eval. 30 (2011) 186-200.

[34] J. Moll, R. T. Schulte, B. Hartmann, C. P. Fritzen, O. Nelles, Multi-site damage localization in anisotropic plate-like structures using an active guided wave structural health monitoring system, Smart Mater. Struct. 19 (2010) 045022.

[35] E. Baravelli, M. Senesi, M. Ruzzene, L. De Marchi, Fabrication and characterization of a wavenumber-spiral frequency-steerable acoustic transducer for source localization in plate structures, IEEE Trans. Instrum. Meas. 62 (2013) 2197-2204.

[36] L. Qiu, B. Liu, S. Yuan, Z. Su, Impact imaging of aircraft composite structure based on a model-independent spatial-wavenumber filter, Ultrasonics 64 (2016) 10-24.

[37] L. Yu, V. Giurgiutiu, In situ 2-D piezoelectric wafer active sensors arrays for guided wave damage detection, Ultrasonics 48 (2008) 117-134.

[38] B. Xu, V. Giurgiutiu, Single mode tuning effects on lamb wave time reversal with piezoelectric wafer active sensors for structural health monitoring, J. Nondestruct. Eval. 26 (2007) 123-134.

[39] P. D. Wilcox, Omni-directional guided wave transducer arrays for the rapid inspection of large areas of plate structures, IEEE Trans. Ultrason. Ferroelectr. Freq. Control 50 (2003) 699-709.

[40] A. Velichko, P.D. Wilcox, Guided wave arrays for high resolution inspection, J. Acoust. Soc. Am. 123 (2008) 186-196.

[41] D. H. Johnson, D. E. Dudgeon, Array signal processing: concepts and techniques, Simon & Schuster, 1992.